# Forming Limit Diagram (FLD) for sheet metal forming applications

# (Revised in May 2021)

## Introduction

Formability is the ability of sheet metal to undergo shape change without failure by necking or tearing [1]. Two types of necking occur in a standard tensile test, namely diffuse and localized necking (Fig. 1a) [1,2,3]. The diffuse necking appears when the maximum engineering stress is reached, as caused by the in-plane instability in the width direction. The strain at diffuse necking is often called **uniform elongation**. Whereas the localized necking is due to the through-thickness instability leading to severe reduction in the local thickness (close to fracture). The strain at localized necking is often between the uniform elongation and total elongation. Here it is called "**uniaxial tensile limit strain**". A forming limit curve (FLC) is a curve of deformation limit generally governed by **localized necking** that associates with ductile fracture. FLC plots the major strain at the onset of localized necking for all values of the minor strain at different loading paths, e.g. uniaxial, equibiaxial, etc, and the full graph is called forming limit diagram (FLD, see Fig. 1b) [2,3,4].



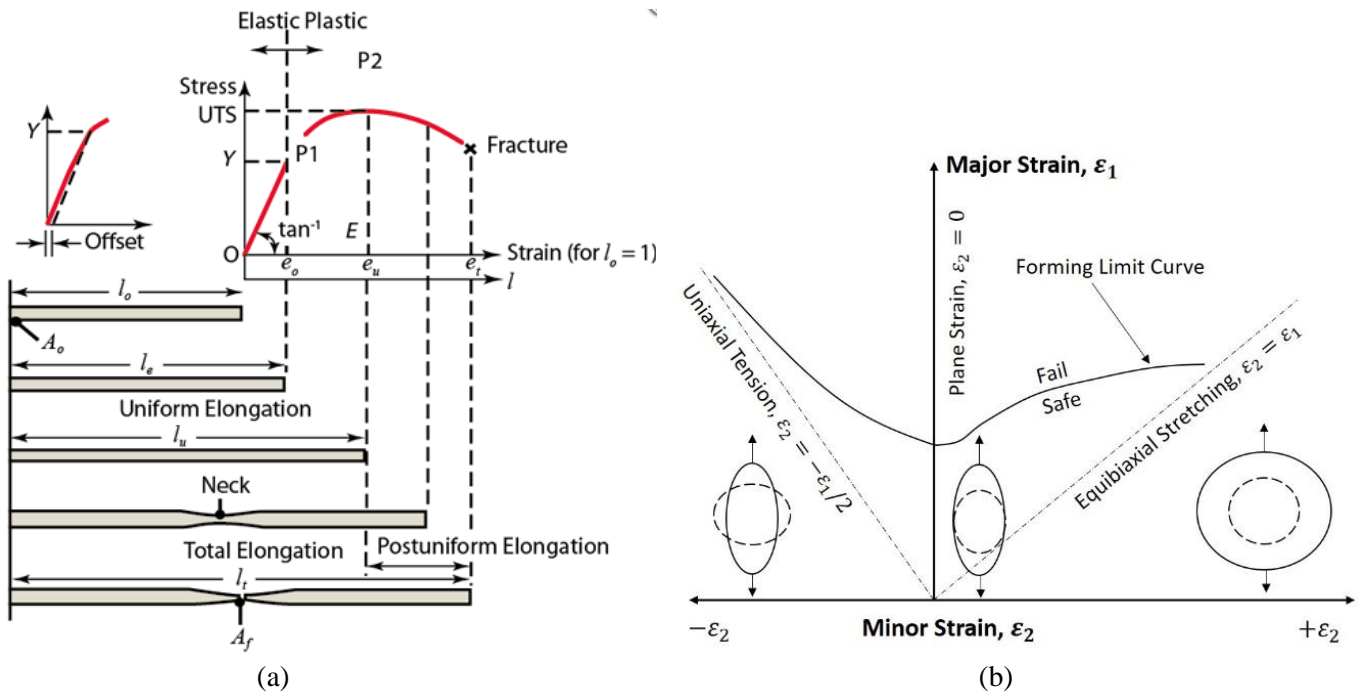(a)                                                    (b)

Fig. 1 (a) Standard tensile test with different elongations; (b) Standard forming limit curve (FLC) obtained by a combination of different loading ratios.

A standard FLD test requires proportional loading conditions, where the ratio of major and minor strain increments ($\alpha = d\varepsilon_2 / d\varepsilon_1$) remains constant throughout the forming process. The elastic strain can be ignored since the forming process often involves large deformation mainly consisting of plastic strain. FLD can be divided into two branches considering the sign of $\alpha$.

1) Left branch, from uniaxial tensile loading to plane strain loading ($\alpha$ from -0.5 to 0 in isotropic condition);
2) Right branch, from plane strain loading to biaxial loading towards equibiaxial stretching ($\alpha$ from 0 to 1).

The two branches match at "plane strain" condition at $\alpha$=0, the lowest point on FLC, or **FLC0**. Beyond the full range of $\alpha$, other fracture mechanisms may occur [2], which is not the concern in this article. Fig. 1(b) illustrates the standard strain-based FLC, which is understood to be history dependent [5] that can shift given pre-existing residual strain (Fig. 2a, Ref. [5]). While the stress-based FLC or forming stress limit curve (FSLC) is found to be history and path-independent (Fig. 2b, Ref [5]). At room temperature without any history effect, FSLC and FLC are considered to be identical representation of the forming limit.
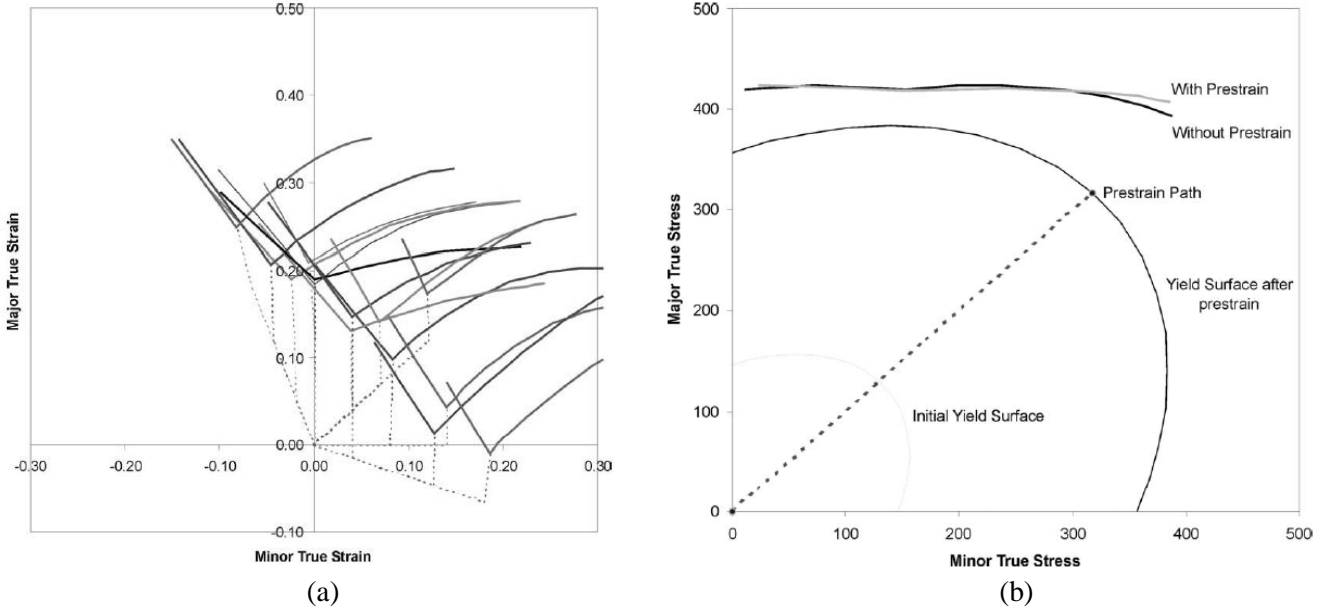
Fig. 2 (a) Schematic changes to FLC with different levels of pre-strain [5]; (b) History and path-independent stress-based FLC [5]

Complexity arises when the sheet metals are strongly anisotropic. Plastic anisotropy of a sheet metal is often measured by the Lankford coefficient, also called R-value. It affects the yield criterion or yield surface that can ultimately influence the formability of the sheet metals. As a further development of the mechanical properties capability for JMatPro®, this article provides an overview of the model incorporated in JMatPro® to calculate both strain-based and stress-based forming limit diagram, based on the existing flow stress curve calculation capability in JMatPro®.

## Modelling of FLD at room temperature

Models used for FLD are different for the left and right branch, but are based on the following assumptions:

1) Non-quadratic Logan-Hosford yield criterion (2D)

$$f^{\,p} = \sigma_{eq}^{\,p} = \frac{1}{1+R}\left(|\sigma_1|^p + |\sigma_2|^p\right) + \frac{R}{1+R}|\sigma_1 - \sigma_2|^p \tag{1}$$

where $\sigma_1$ and $\sigma_2$ are the major and minor principal true stresses, $\sigma_{eq}$ is the equivalent true stress, $R$ is Lankford coefficient ($R=1$ if isotropic) and $p$ is the order of yield surface typically between 2 and 12. Here only the single normal R-value is used. When $R=1$, $p=2$, it simplifies into the popular quadratic Von Mises isotropic yield criterion.

$$f = \sigma_{eq} = \sqrt{\sigma_1^{\,2} + \sigma_2^{\,2} - \sigma_1\sigma_2} \tag{2}$$

Figure 3 illustrates some example yield surfaces for plane stress problems given the same uniaxial yield strength but different values of $R$ or $p$. It should be noted that although the yield surfaces with different values of $p$ are not far apart, the strain-based FLD can be significantly different, which will be illustrated later in the result evaluation.
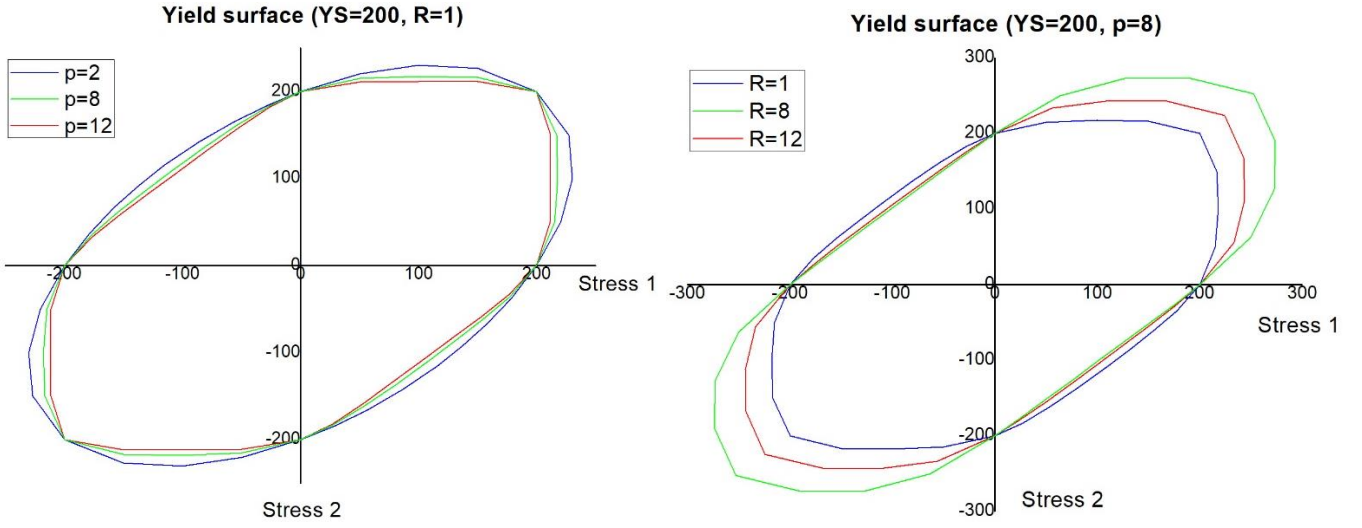
Fig. 3 Schematic 2D yield surface at 200MPa equivalent yield stress: (a) when R=1 but p varies; (b) when p=8 but R varies.

2) Plastic flow rule

$$d\varepsilon = d\lambda \frac{df}{d\sigma} \tag{3}$$

where $d\lambda$ is the proportionality constant equal to the effective strain increment $d\varepsilon_{eq}$. Under Von Mises yield criterion, $d\varepsilon_{eq} = 2/\sqrt{3}\sqrt{d\varepsilon_1^2 + d\varepsilon_1 d\varepsilon_2 + d\varepsilon_2^2} = 2/\sqrt{3}\, d\varepsilon_1\sqrt{1 + \alpha + \alpha^2}$

3) Power-law constitutive law (*n*: hardening exponent; *K*: strength coefficient)

$$\sigma_{eq} = K\varepsilon_{eq}{}^{n} \tag{4}$$

## 1. Left branch of FLD

In a standard uniaxial tensile test, the uniform elongation (true strain) can be approximated to be equal to the hardening exponent *n*. Hill [2,6] extends this to describe the strain at localized necking of sheet metals, assuming a local neck will form at the zero extension direction. The reduction in thickness and effect of hardening balance each other when the neck forms, i.e. the fractions within the material reach a state where the traction increments equal to zero. The zero extension direction has been derived with an angle $\varphi = \tan^{-1}\sqrt{-\alpha}$ to the direction of the major principal stress. Therefore, Hill's model is physically valid only when α<0 thus it can only be used for the left branch of FLD. Hill then derived the following criterion and the expression of the major and minor strain of FLC.

$$\frac{d\sigma_t}{d\varepsilon_t} = \sigma_t\left(1+\alpha\right) \rightarrow \varepsilon_t = \frac{n}{1+\alpha} \rightarrow \begin{cases} \varepsilon_{major} = \dfrac{n}{1+\alpha} \\[2mm] \varepsilon_{minor} = \dfrac{\alpha n}{1+\alpha} \end{cases} \rightarrow \begin{cases} \varepsilon_{major} = \dfrac{\varepsilon_p}{1+\alpha} \\[2mm] \varepsilon_{minor} = \dfrac{\alpha\varepsilon_p}{1+\alpha} \end{cases} \tag{5}$$

where the subscript "*t*" represents true stress/strain. Note we have replaced *n* with a characteristic elongation term $\varepsilon_p$, which provides some flexibilities in the calculation and further calibration as many factors may cause a shift in FLC, such as sheet thickness (a standard value is ~1mm) [7], forming speed (or strain rate) and temperature [3,4]. The strain rate and temperature effect is tackled later, while the thickness effect is out of the scope of this article. In addition, note that Hill's theory for the left branch of strain-based FLD is independent of the Lankford coefficient *R* and the order of yield surface *p*.

In Eq. (5), the characteristic term $\varepsilon_p$ is equivalent to FLC0 when α=0 (Fig. 1b). In a generalized condition, $\alpha = -R/(1+R)$ represents uniaxial tensile loading direction, hence the localized necking occurs at $(1+R)\varepsilon_p$. In the specific isotropic condition (*R*=1), $\alpha = -0.5$ represents uniaxial tensile loading direction and the

localized necking occurs at $2\varepsilon_p$. If all other factors (e.g. sheet thickness, strain rate and temperature) can be ignored, $(1 + R)\varepsilon_p$ in FLD can be approximated to be the **uniaxial tensile limit strain** (Fig. 1a) obtained from a standard uniaxial tensile test (although specimens and procedures of the two tests are different). Combining Eqs. (1) and (3)-(5), the corresponding stress-based FLD can be obtained. Different from the strain-based FLD (Eq. 5), choice of $R$ and $p$ would affect the stress-based FLD. Eq. (6) shows the expressions at isotropic condition ($R=1$, $p=2$) while the general expressions are ignored in this article due to complexity.

$$\begin{cases} \sigma_{major} = \dfrac{K(2+\alpha)}{\sqrt{3}\sqrt{1+\alpha+\alpha^2}} \left( \dfrac{2\varepsilon_p \sqrt{1+\alpha+\alpha^2}}{\sqrt{3}(1+\alpha)} \right)^n \\[4mm] \sigma_{minor} = \dfrac{K(1+2\alpha)}{\sqrt{3}\sqrt{1+\alpha+\alpha^2}} \left( \dfrac{2\varepsilon_p \sqrt{1+\alpha+\alpha^2}}{\sqrt{3}(1+\alpha)} \right)^n \end{cases} \tag{6}$$

## 2. Right branch of FLD

For the right branch of biaxial stretching, two theories are applied to better describe the formability of sheet metals made from different materials. Firstly, the Bressan-William (BW) theory [8] assumes that the instability starts when the local shear stress along the pure shear strain direction exceeds a critical value, which can be predicted from the major principal stress simply from Mohr's circle.

$$\tau_{cr} = \frac{\sigma_1}{2} \sin 2\theta = \frac{\sigma_1}{2} \sqrt{1 - \cos^2 2\theta} = \sigma_1 \frac{\sqrt{\alpha+1}}{\alpha+2} \tag{7}$$

where $\cos 2\theta = -\alpha/(\alpha+2)$ represents the orientation of the plane of critical shear stress. Expressions of the right branch of the stress-based FLD are firstly determined by matching the BW criterion and the modified Hill expression (Eq. 6) at the plane strain condition ($\alpha = 0$) and calibrating the critical shear stress. Then it is combined with Eqs. (1), (3) and (4) to obtain the expressions of the strain-based FLD. Eqs. (8) and (9) are the expressions at isotropic condition ($R=1$, $p=2$) while the general expressions are ignored due to complexity.

$$\left(\tau_{cr}\right)_{\alpha=0} = \frac{1}{\sqrt{3}} K \left( \frac{2\varepsilon_p}{\sqrt{3}} \right)^n \rightarrow \begin{cases} \sigma_{major} = \dfrac{K(2+\alpha)}{\sqrt{3}\sqrt{1+\alpha}} \left( \dfrac{2\varepsilon_p}{\sqrt{3}} \right)^n \\[4mm] \sigma_{minor} = \dfrac{K(1+2\alpha)}{\sqrt{3}\sqrt{1+\alpha}} \left( \dfrac{2\varepsilon_p}{\sqrt{3}} \right)^n \end{cases} \tag{8}$$

$$\begin{cases} \varepsilon_{major} = \dfrac{\varepsilon_p}{\sqrt{1+\alpha+\alpha^2}} \left( \dfrac{\sqrt{1+\alpha+\alpha^2}}{\sqrt{1+\alpha}} \right)^{1/n} \\[4mm] \varepsilon_{minor} = \dfrac{\alpha\varepsilon_p}{\sqrt{1+\alpha+\alpha^2}} \left( \dfrac{\sqrt{1+\alpha+\alpha^2}}{\sqrt{1+\alpha}} \right)^{1/n} \end{cases} \tag{9}$$

The second theory is the Storen-Rice (SR) bifurcation or vertex theory [2-5]. It assumes that the instability starts when a bifurcation or vertex, as associated with the uncertain direction of plastic flow which triggers inhomogeneous deformation, eventually develops on a yield surface. Eqs. (10) and (11) are the expressions of strain- and stress-based FLD at isotropic condition ($R=1$, $p=2$) using this theory.

$$\begin{cases} \varepsilon_{major} = \dfrac{3\alpha^2 + n(2+\alpha)^2}{2(2+\alpha)(1+\alpha+\alpha^2)} \cdot \dfrac{\varepsilon_p}{n} \\[3mm] \varepsilon_{minor} = \dfrac{\alpha\left(3\alpha^2 + n(2+\alpha)^2\right)}{2(2+\alpha)(1+\alpha+\alpha^2)} \cdot \dfrac{\varepsilon_p}{n} \end{cases} \tag{10}$$

$$\begin{cases} \sigma_{major} = \dfrac{K(2+\alpha)}{\sqrt{3}\sqrt{1+\alpha+\alpha^2}} \left( \dfrac{3\alpha^2 + n(2+\alpha)^2}{(2+\alpha)\sqrt{3(1+\alpha+\alpha^2)}} \cdot \dfrac{\varepsilon_p}{n} \right)^n \\[4mm] \sigma_{minor} = \dfrac{K(1+2\alpha)}{\sqrt{3}\sqrt{1+\alpha+\alpha^2}} \left( \dfrac{3\alpha^2 + n(2+\alpha)^2}{(2+\alpha)\sqrt{3(1+\alpha+\alpha^2)}} \cdot \dfrac{\varepsilon_p}{n} \right)^n \end{cases} \tag{11}$$

where the term $\varepsilon_p/n$ is incorporated to allow flexibility in the FLC0 calculation, similar to the Hill and BW models.

Other models for the right branch exist, such as the Swift biaxial diffuse necking criterion [2] and the Tresca maximum shear stress criterion [2]. The former assumes that instability starts when diffuse necking occurs along both principal directions of stress, while the latter assumes that instability starts when the maximum shear stress exceeds a critical value. However, these theories have been shown to be less consistent with data compared with BW and SR theories [2]. A well-known universal theory applicable for the entire FLD is the Marciniak-Kuczynski (MK) geometrical imperfection theory [3,4]. This theory postulates an initial groove, which contains an initial defect characterized by either a geometric variation in the thickness with some physical connection with the initial porosity [9] or material non-uniformity in the hardening exponent [7]. The MK theory assumes that instability starts when the defect has grown extensively to a critical ratio compared with that of the "healthy" region. FLD is determined by fitting a new parameter to the data, named initial inhomogeneity of thickness. However, quite a few studies [3,4] have complained about the over-sensitive nature of this new parameter.

The combination of the modified Hill and Bressan-William (HBW) criterion or Storen-Rice (HSR) criterion are the fundamental framework of FLD calculation in JMatPro®, with four governing parameters ($n$, $R$, $p$ and $\varepsilon_p$) while the loading ratio $\alpha$ is a known parameter in the forming process. Among these four parameters, $n$ and $R$ influence the entire shape of FLD, $p$ only affects the right branch, while $\varepsilon_p$ plays the role of shifting and scaling the entire FLD. It is apparent that the prerequisite for FLD computation is the flow stress curve calculation, which is available in JMatPro®. For the applicability of these combined models, HSR is used for Al, Ti and Mg alloys, while HBW is used for other materials (e.g. Ni and Fe alloys).

**Evaluation of FLD at room temperature (RT)**

In this section, we evaluate the strain-based FLD at room temperature (RT). In the literature, Al and Fe alloys have been the most popular alloy types with FLD applications. An extensive data collection of FLC0 and $n$ of a series of Al and Fe alloys from literature [2,7,10-18] (with ~1 mm thickness) show that the average FLC0 is ~ $n$ for Al alloys and ~ 1.5 $n$ for Fe alloys. These have been found to be generally consistent with the uniaxial tensile limit strain obtained from the flow stress curve calculation in JMatPro®.

FLD of several example Al and Fe alloys at RT are calculated and shown in Fig. 4 (for Al) and Fig. 5 (for Fe). An empirical relationship [2,7] is used to shift the reported FLD results if the sheet thickness is notably different from 1 mm. Good matches can be observed in all the alloys in Figs. 4 and 5. Note many calculated FLDs have covered a wider range of strain compared with the experimental data. This may be due to incomplete tests not covering the full range of loading ratios.
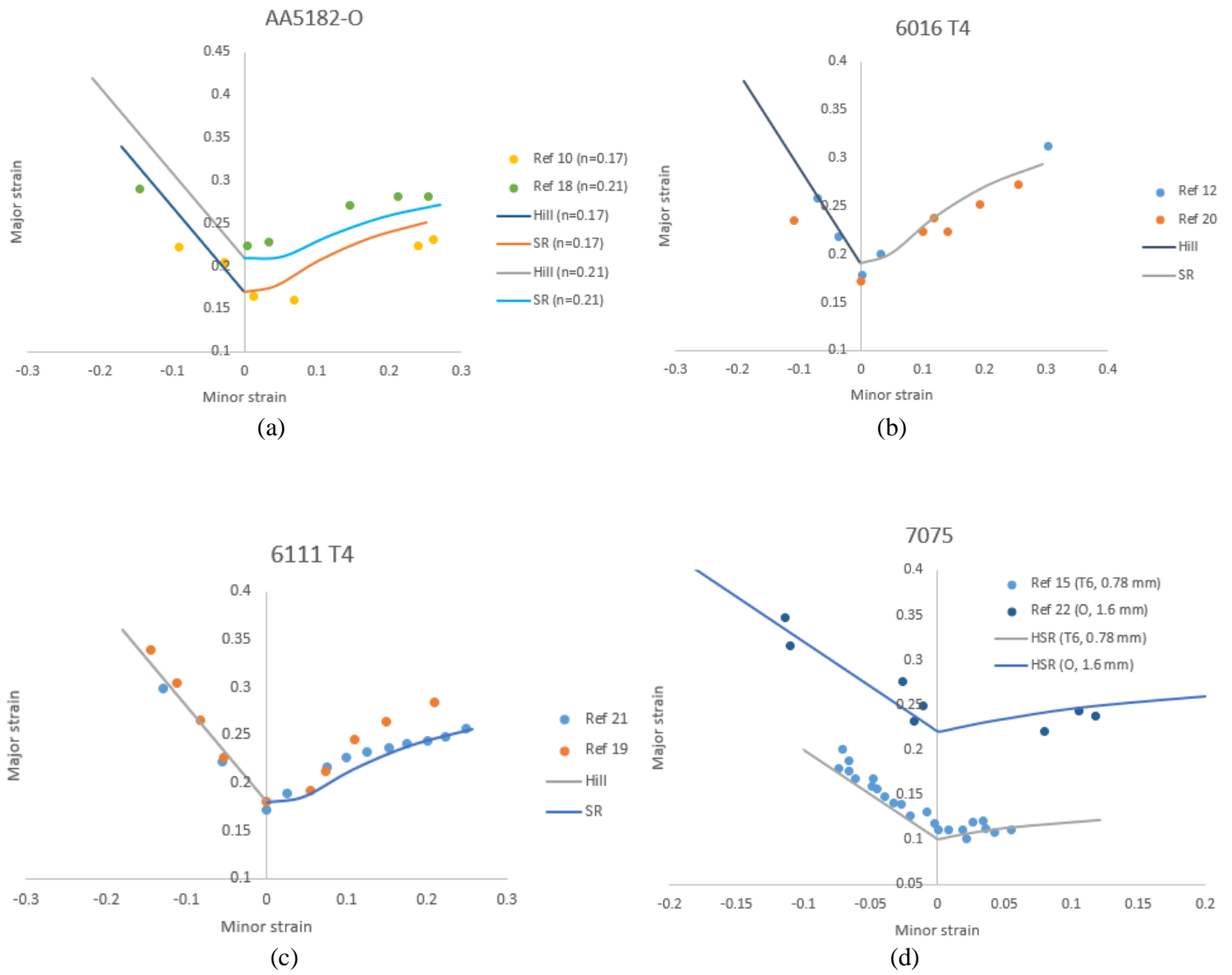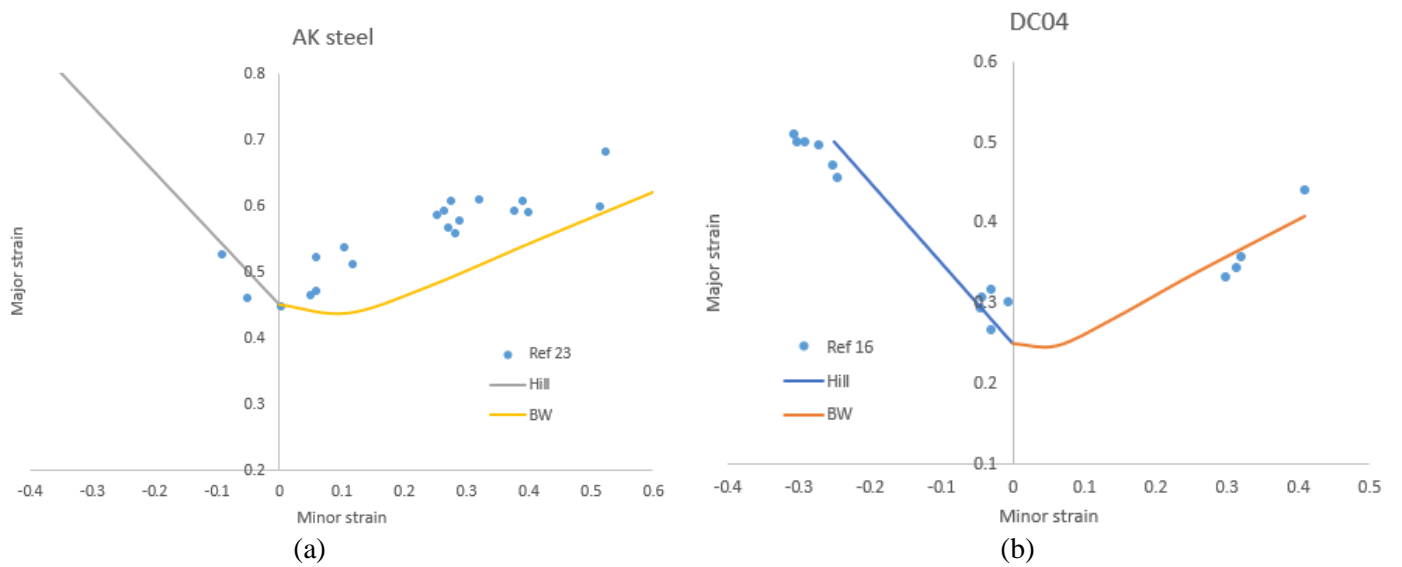
Fig. 4 Comparison of measured and calculated room temperature FLD of four example Al alloys: (a) AA5182-O; (2) 6016-T4; (c) 6111-T4; (d) 7075-T6 (0.78 mm thickness) and 7075-O (1.6 mm thickness)
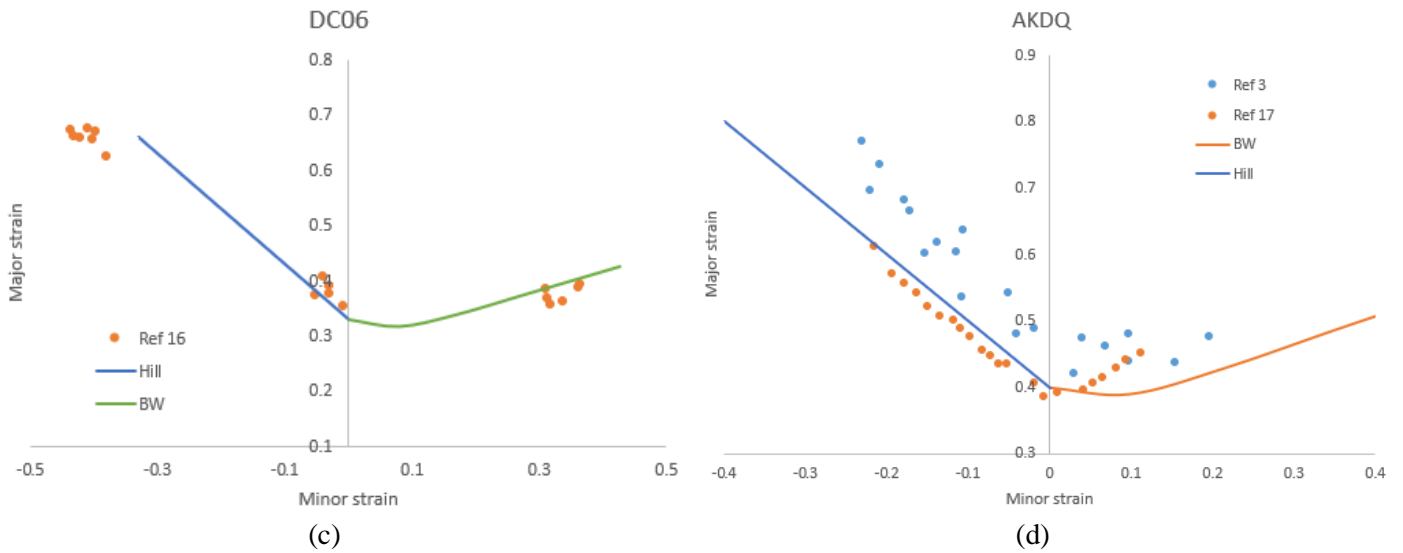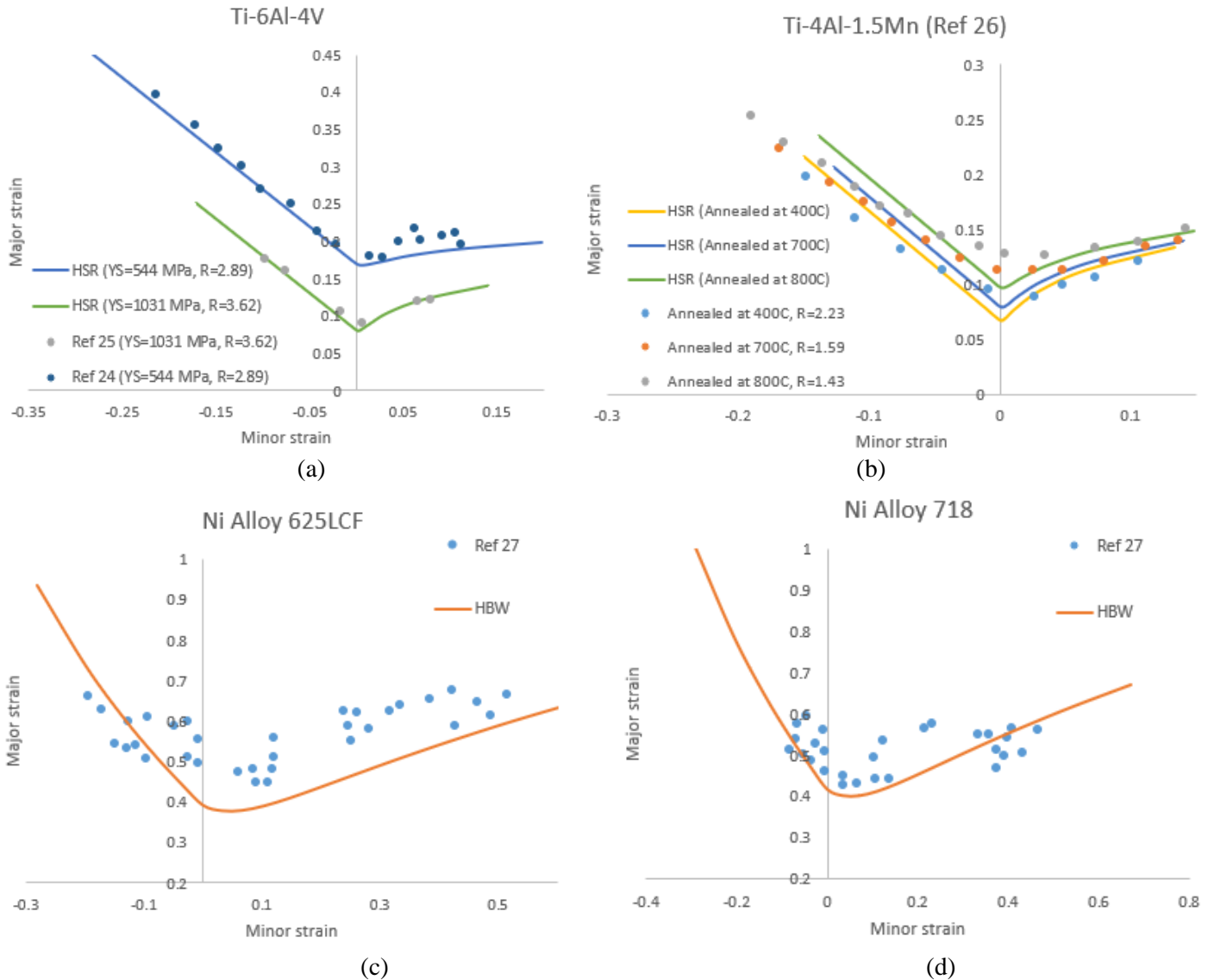
Fig. 5 Comparison of measured and calculated room temperature FLD of four example Fe alloys: (a) AK steel; (b) DC04; (c) DC06; (d) AKDQ

Apart from Al and Fe alloys, the justified approach also works for other types of alloys. Fig. 6 shows the good agreement between the measured and calculated FLD at RT of some Ti, Ni, Mg alloys and stainless steel.

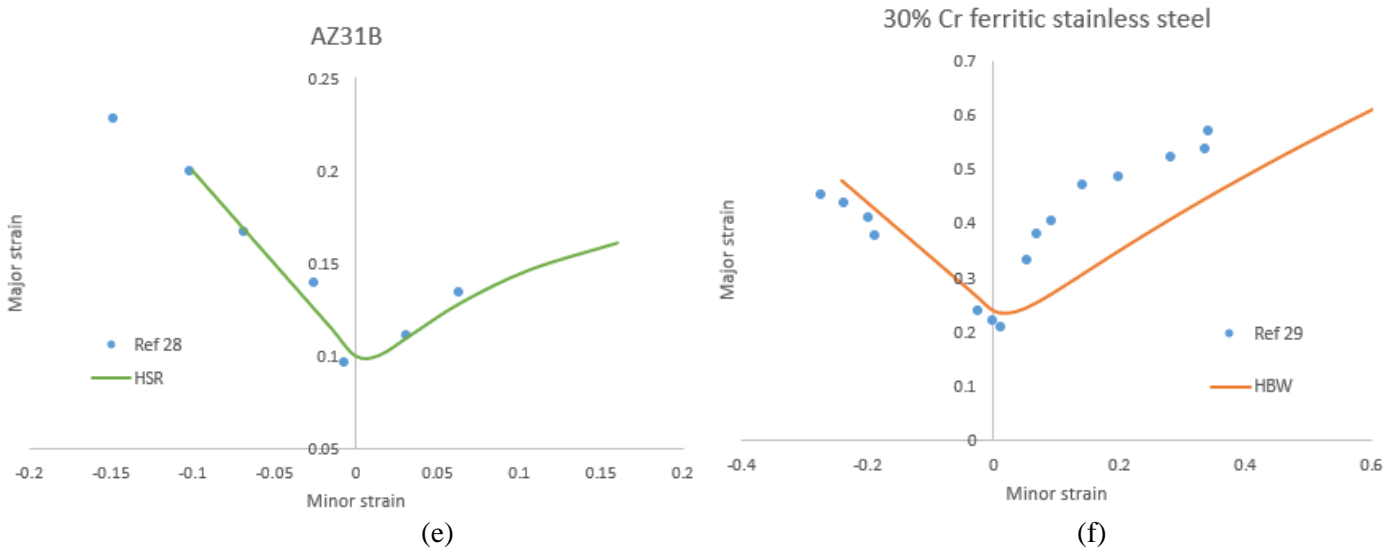(e)                                                    (f)

Fig. 6 Comparison of measured and calculated room temperature FLD for: (a) Ti-6Al-4V; (b) Ti-4Al-5Mn; (c) Ni alloy 625LCF; (d) Ni alloy 718; (e) Mg-3Al-1Zn (AZ31B); (f) 30% Cr ferritic stainless steel

Among these sheet metal alloys, only Ti alloys have exhibited a high degree of anisotropy (Fig. 6a and b, R-value much higher than 1). Fig. 7(a) shows the FLD data of a Ti-5Al-2.5Sn alloy sheet with very strong anisotropy ($R=12$) or texture. The calculated FLD results with different $R$ values are presented for a comparison, the order of yield surface has been fixed to be 6. FLC0 has been slightly shifted to distinguish the forming limit curves with different $R$ values. Apparently, the increase of $R$ value or the degree of texture appears to enhance the formability mainly in the left branch, i.e. when the loading ratio is below 0, compared with the right branch. This enhancement in formability can be explained using Hill's left branch FLD model. As previously mentioned, at isotropic condition ($R=1$), the uniaxial loading ratio is -0.5 thus the major strain is $2\varepsilon_p$. At strongly anisotropic condition (e.g. $R=12$), the uniaxial loading ratio is $-R/(1+R) \approx -0.923$ thus the major strain would become approximately $13\varepsilon_p$.

Figure 7(b) presents the FLD data of an annealed Mg alloy (ZEK100-O) sheet with negligible anisotropy ($R=0.79$). The calculated FLD results with different $p$ values are presented for comparison. Apparently, the increase of $p$ value appears to reduce the formability in the right branch, i.e. when the loading ratio is above 0, compared with the left branch. For this Mg alloy sheet, it is observed that $p=12$ matches the best to the data. This reduction of formability can be originated from the yield surface illustrated in Fig. 3(a), which shrinks as the order increases.
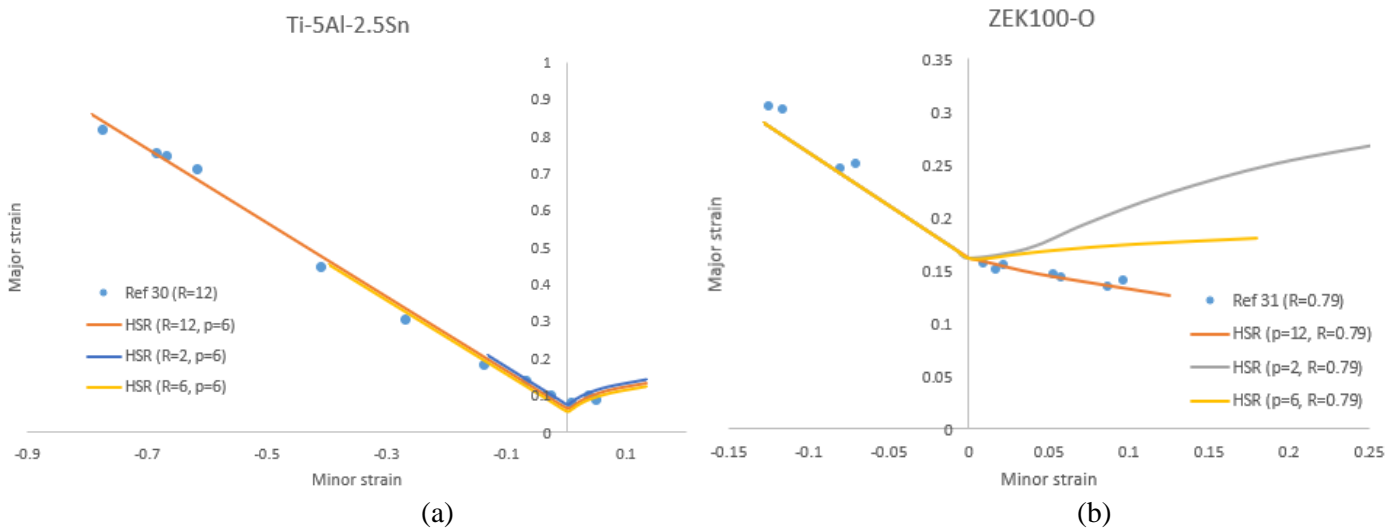




(a)                                                    (b)

Fig. 7 Evaluation of room temperature FLD for: (a) Ti-5Al-2.5Sn with variation in anisotropy R-value (curves have been shifted for a better comparison); (b) Mg ZEK100-O with variation in the order of yield surface.

## Modelling of FLD at elevated temperatures

The formability of sheet metals has been found to increase with temperature during warm/hot forming processes. However, determining FLDs experimentally at warm/hot forming conditions is technically difficult, time-consuming and costly, thus data of FLD at elevated temperatures is much less available compared with the RT counterpart. One significant complexity is the forming speed or strain rate sensitivity during this warm/hot forming process. From the modelling perspective, one way of incorporating the strain rate sensitivity is by modifying Eq. (4) into the following expression.

$$\sigma_{eq} = K\varepsilon_{eq}{}^{n}\left(\dot{\varepsilon}_{eq}/\dot{\varepsilon}_0\right)^{m} \tag{12}$$

where $m$ is called the strain rate sensitivity factor, $\dot{\varepsilon}_0$ is a reference strain rate. However, uncertainty for the FLD calculation increases due to the following additional complexities:
- $K$, $n$ and $m$ are all temperature-dependent;
- $m$ is often considered to be a constant, but its value is rather an approximation (obtained at a certain value of strain from two tests with different strain rates, $m = \ln(\sigma_2/\sigma_1)/\ln(\dot{\varepsilon}_2/\dot{\varepsilon}_1)$);
- In the FLD experiment, constant forming speed does not infer constant strain rate at all times and regions, thus the enhanced strain rate sensitivity of the sample at elevated temperatures is difficult to describe with a single equation.

In the literature, SR and Marciniak-Kuczynski (MK) theories have been extended to combine with Eq. (12) to calculate FLD at elevated temperatures [3,4]. However, both extensions contain an additional fitting parameter and are rather case-sensitive requiring careful calibration, considering the above uncertainties.

In JMatPro®, the strain rate sensitivity of the flow stress behaviour at elevated temperatures is treated differently, considering that defects (dislocations and voids) can be generated more slowly at elevated temperatures and the deformation mechanism may change from dislocation glide to dislocation climb, i.e. creep flow softening may dominate [32,33]. In addition, the enhanced mobility of defects helps alleviate, to some extent, the residual stress and the concentration of defects at certain regions. All of these can lead to a delayed localized necking due to the competition between strengthening and softening.

Here we explore the capability of the modified HBW and HSR criteria, combined with the temperature-dependent flow stress curve functionality in JMatPro®, to deal with FLD at elevated temperatures. The approach remains generally the same as described before, except that the **uniaxial tensile limit strain** is determined with the aid of a modified Clift ductile fracture-based criteria [34]:

$$\int_0^{2\varepsilon_p} \sigma d\varepsilon = C \tag{13}$$

where $C$ is a material-specific constant. It is obtained from the calculated flow stress curve at RT at the reference strain rate with readily known uniaxial tensile limit strain. Then it is combined with the flow stress curve at the actual temperature and strain rate to calculate the actual limit strain and FLC0 (or $\varepsilon_p$). Finally this FLC0 is used in the modified HBW or HSR criteria to determine the entire FLD.

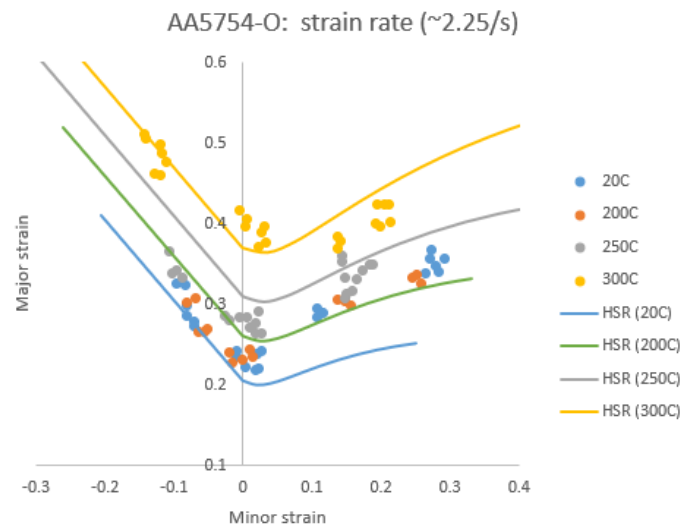## Evaluation of FLD at elevated temperatures

The FLDs of some available Al and Fe sheet metal alloys in literature at elevated temperatures are examined in this section. An initial comparison has been made between the reported and calculated FLC0s at various temperatures and strain rates [35-52]. By scaling the FLC0s of some alloys tested outside the standard thickness range using an empirical relationship [2], it is found that the majority of the calculated FLC0s match reasonably well within 30% of the reported values.

The entire FLC results of some example Al and Fe sheet metals at various temperatures and strain rates are presented in Fig. 8 [35-43]. Note the constant strain rate used in JMatPro® is either the reported approximated value or estimated from the reported forming speed. The general trends are captured reasonably well. It can be found that the predicted FLC0 as well as the entire FLC consistently shifts up with increasing temperature at a given strain rate, or with decreasing strain rate at a given temperature. Note in these calculations, all the sheet metals have been assumed to be isotropic ($R$=1) with the simple Von Mises yield criterion ($p$=2) due to

lack of the anisotropy information in the literature. However, the discrepancy of the calculated FLDs compared with the reported results can be compensated by calibration with the actual experimental uniaxial tensile limit strain or a pair of major-minor strains at any given loading ratio. The calibration procedure is optional in JMatPro® and is ignored in this report.
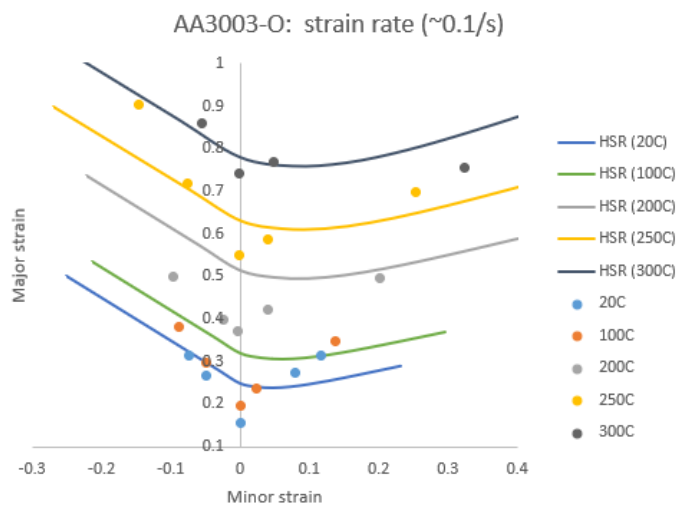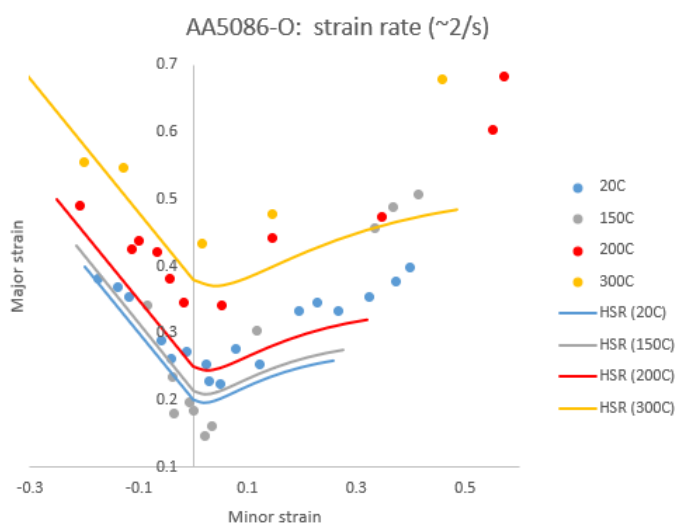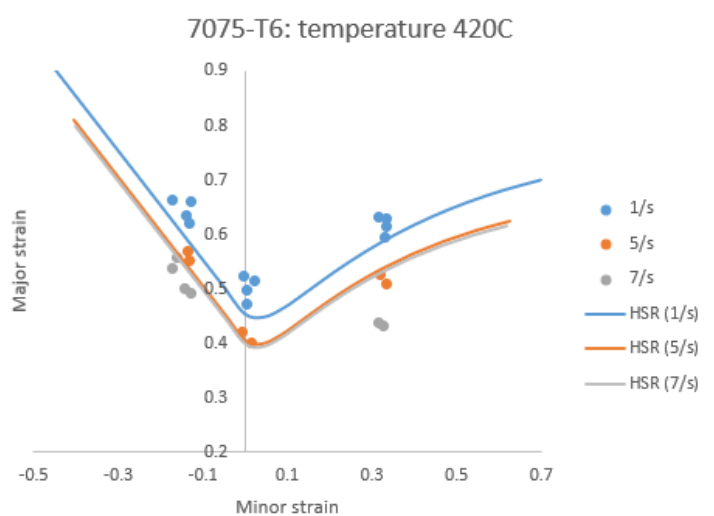


(a)

(b)

(c)

(d)

(e)

(f)

(g)                                                                          (h)
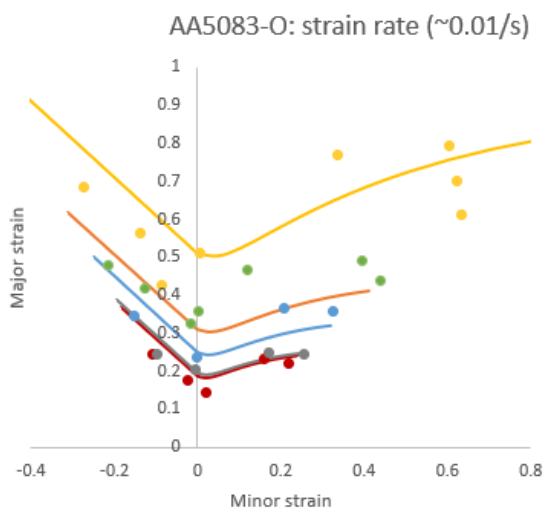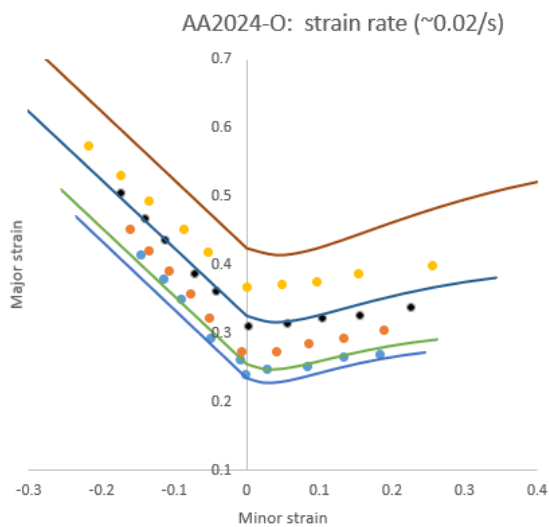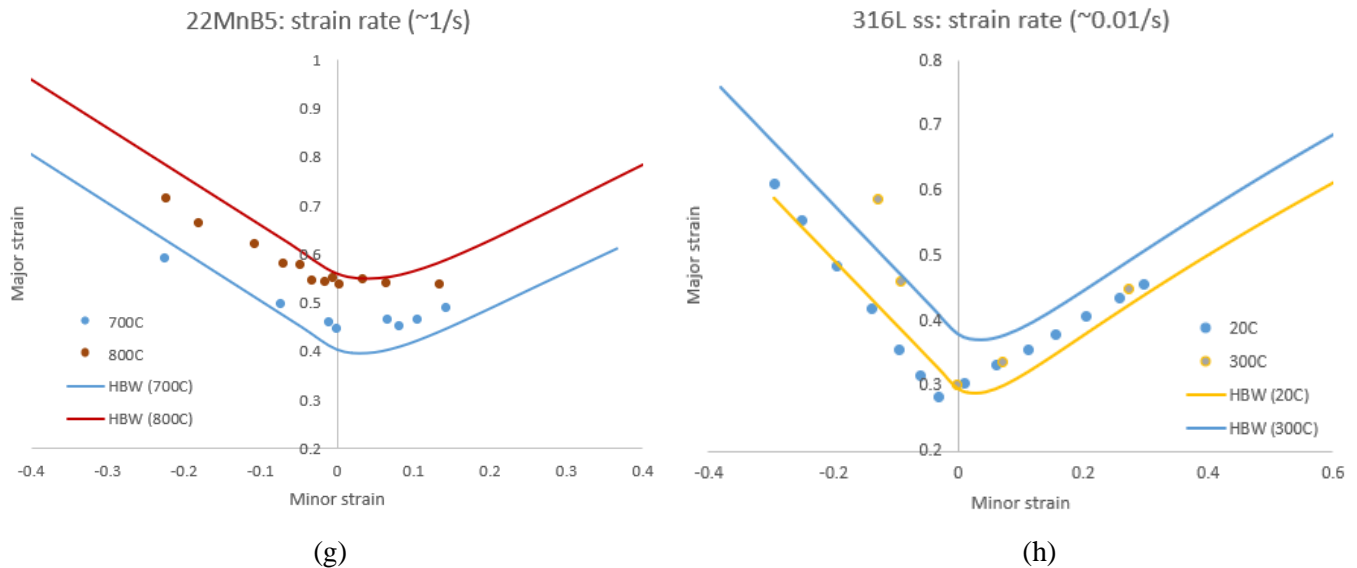
Fig. 8 Evaluation of FLD of example Al and Fe alloys at varying strain rates and elevated temperatures (solid points: experimental data; solid lines: simulated results) (a) Al, AA5083-O at fixed strain rate (~0.01/s) [35]; (b) Al, AA5754-O at fixed strain rate (~2.25/s) [36]; (c) Al, AA2024-O at fixed strain rate (~0.01/s) [39]; (d) Al, AA3003-O at fixed strain rate (~0.1/s) [38]; (e) Al, AA5086-O at fixed strain rate (~2/s) [37]; (f) Al, AA7075-T6 at fixed temperature (420°C) [40]; (g) Fe, 22MnB5 at fixed strain rate (~3/s) [41]; (h) Fe, 316L stainless steel at fixed strain rate (~0.01/s) [42,43].

## Conclusion

To summarize, the forming limit diagram (FLD) calculation for a range of alloys is explored. Capabilities of several analytical FLD models are evaluated, namely the modified Hill zero extension theory for the left branch, and the Bressan-William (BW) shear instability theory as well as the Storen-Rice (SR) bifurcation theory for the right branch. The anisotropy complexities are also embedded in these theories. The joint HBW and HSR criteria, combined with the existing flow stress curve capability in JMatPro®, have been shown to agree well with the collected experimental data. The approach, with the aid of a modified Clift ductile fracture criterion, is also capable of tackling the effect of varying strain rates and temperatures on FLD. It provides further insight on the correlation between the tensile flow behavior and formability of a given material, and can be applied to aid the materials selection in industry regarding the sheet metal forming.

## References

1. https://en.wikipedia.org/wiki/Forming_limit_diagram
2. Paul, S.K. Theoretical analysis of strain-and stress-based forming limit diagrams. *J Strain Analysis*. 2013, 48(3): 177-188.
3. Jie, M., Cheng, C.H., Chan, L.C., Chow, C.L. Forming limit diagrams of strain-rate-dependent sheet metals. *Int. J. Mech. Sci*. 2009, 51: 269-275.
4. Min, J. Lin, J., Li, J., Bao, W. Investigation on hot forming limits of high strength steel 22MnB5. *Comp Mater Sci*. 2010, 49: 326-332.
5. Stoughton, T.B., Zhu X. Review of theoretical models of the strain-based FLD and their relevance to the stress-based FLD. *Int J Plast*. 2004, 20: 1463-1486.
6. Hill, R. On discontinuous plastic states with special reference to localized necking in thin sheets. *J Mech Phys Solids*. 1952, 1: 19-30.
7. Ghazanfari, A., Assempour, A. Calibration of forming limit diagrams using a modified Marciniak-Kuczynski model and an empirical law. *Mater Des*. 2012, 34: 185-191.
8. Bressan, J.D., William, J.A. The use of a shear instability criterion to predict local necking in sheet metal deformation. *Int. J. Mech. Sciences*. 1983, 25: 155-168.
9. Barlat, F., Richmond, O. Modelling macroscopic imperfections for the prediction of flow localization and fracture. *Fatigue Fract Engng Mater Struct*. 2003, 26: 311-321.
10. Brunet, M., Mguil, S., Morestin, F. Analytical and experimental studies of necking in sheet metal forming processes. *J. Mater. Process. Technol*. 1998, 80-81: 40-46.

11. Ahmadi, S., Eivani, A.R., Akbarzadeh, A. An experimental and theoretical study on the prediction of forming limit diagrams using new BBC yield criteria and M-K analysis. *Comp. Mater. Sci*. 2009, 44: 1272-1280.

12. Banabic, D., Lazarescu, L., Paraianu, L., Ciobanu, I., Nicodim, I., Comsa, D.S. Development of a new procedure for the experimental determination of the forming limit curves. *CIRP Annals – Manufacturing Technology*. 2013, 62: 255-258.

13. Turkoz, M., Yigit, O., Dilmec, M., Halkaci, H.S. Construction of forming limit diagrams for AA 5754 and AA 2024 aluminium alloys. *Proceedings of the 12<sup>th</sup> International Conference on Aluminium Alloys*. 2010: 516-521.

14. Janbakhsh, M., Djavanroodi, F., Riahi, M. A comparative study on determination of forming limit diagrams for industrial aluminium sheet alloys considering combined effect of strain path, anisotropy and yield locus. *J Strain Analysis*. 2012, 47(6): 350-361.

15. Janbakhsh, M., Loghmanian, S.M.R., Djavanroodi, F. Application of different Hill's yield criteria to predict limit strains for aerospace titanium and aluminium sheet alloys. *Int J Advanced Design and Manufacturing Technology*. 2014, 7: 35-44.

16. Janssens, K., Lambert, F., Vanrostenberghe, S., Vermeulen, M. Statistical evaluation of the uncertainty of experimentally characterised forming limits of sheet steel. *J Mater. Process. Tech*. 2001, 112: 174-184.

17. Strano, M., Colosimo, B.M. Logistic regression analysis for experimental determination of forming limit diagrams. *Int. J Mach. Tool. Manu*. 2006, 46: 673-682.

18. Takuda, H., Mori, K., Takakura, N., Yamaguchi, K. Finite element analysis of limit strains in biaxial stretching of sheet metals allowing for ductile fracture. *Int. J. Mech. Sci*. 2000, 42: 785-798.

19. Signorelli, J.W., Bertinetti, M.A., Turner, P.A. Predictions of forming limit diagrams using a rate-dependent polycrystal self-consistent plasticity model. *Int J. Plast*. 2009, 25: 1-25.

20. Butuc, M.C., Gracio, J.J., da Rocha, A.B. An experimental and theoretical analysis on the application of stress-based forming limit criterion. *Int. J. Mech. Sciences*. 2006, 48: 414-429.

21. Chow, C.L., Yang, X.J., Chu, E. Prediction of forming limit diagram based on damage coupled kinematic-isotropic hardening model under nonproportional loading. *J. Eng. Mater. Technol*. 2002, 124: 259-265.

22. Martinez-Donaire, A.J., Garcia-Lomas, F.J., Vallellano, C. New approaches to detect the onset of localised necking in sheets under through-thickness strain gradients. *Mater. Des*. 2014, 57: 135-145.

23. Ganjiani, M., Assempour, A. An improved analytical approach for determination of forming limit diagrams considering the effects of yield functions. *J. Mater. Process. Tech*. 2007, 18: 598-607.

24. Djavanroodi, F., Derogar, A. Experimental and numerical evaluation of forming limit diagram for Ti6Al4V titanium and Al6061-T6 aluminum alloys sheets. *Mater. Des*. 2010, 31: 4866-4875.

25. Badr, O.M.M.M. Forming behaviour analysis and constitutive modelling of Ti-6Al-4V at room temperature. *PhD thesis for Deakin University*. 2014.

26. Stachowicz, F. Effect of annealing temperature on plastic flow properties and forming limit diagrams of titanium and titanium alloy sheets. *Trans. Jpn. Inst. Met*. 1988, 29(6): 484-493.

27. Roamer, P., Van Tyne, C.J., Matlock, D.K., Meier, A.M., Ruble, H., Suarez, F. Room temperature formability of alloys 625LCF, 718 and 718SPF. *Proceedings of TMS, Superalloys*, 1997, 315-329.

28. Kim, H.J., Choi, S.C., Lee, K.T., Kim, H.Y. Experimental determination fo forming limit diagram and springback characteristics of AZ31B Mg alloy sheets at elevated temperatures. *Mater. Trans*. 2008, 49(5): 1112-1119.

29. Bong, H.J., Barlat, F., Lee, M.G., Ahn, D.C. The forming limit diagram of ferritic stainless steel sheets: experiments and modelling. *Int. J. Mech. Sciences*. 2012, 64: 1-10.

30. Chan, K.S., Koss, D.A. Stretch forming and fracture of strongly textured Ti alloy sheets. *Metall. Trans. A*. 1983, 14A: 1343-1348.

31. Min, J., Hector, L.G., Lin, J.P., Carter, J.T. Analytical methods for forming limit diagram prediction with application to a Magnesium ZEK-O alloy. *J. Mater. Eng. Perform*. 2013, 22(11): 3324-3336.

32. Guo, Z., Saunders. N., Miodownik, A.P., Schille, J.P. Quantification of high temperature strength of nickel-based superalloys. *Mater. Sci. Forum*. 2007, 546-549: 1319-1326.

33. Guo, Z., Saunders, N., Schille, J.P., Miodownik, A.P. Modelling high temperature flow stress curves of titanium alloys. *Proceedings of MRS Conference*. 2008.

34. Clift, S.E., Hartley, P., Sturgess, C.E.N., Rowe, G.W. Fracture prediction in plastic deformation processes. *Int. J. Mech. Sciences*. 1990, 32(1): 1-17.

35. Naka, T., Torikai, G., Hino, R., Yoshida, F. The effects of temperature and forming speed on the forming limit diagram for type 5083 aluminum-magnesium alloy sheet. *J. Mater. Process. Tech*. 2001, 113: 648-653.

36. Shao, Z., Bai, Q., Li, N., Lin, J., Shi, Z., Stanton, M., Watson, D., Dean, T. Experimental investigation of forming limit curves and deformation features in warm forming of an aluminium alloy. *Proceedings of the Institution of Mechanical Engineers, Part B: Journal of Engineering Manufacture*. 2016, 232(3), 465-474.

37. Zhang, C., Chu, X., Guines, D., Leotoing, L., Ding, J., Zhao, G. Effects of temperature and strain rate on the forming limit curves of AA5086 sheet. *Procedia Engineering*. 2014, 81: 772-778.

38. Bagheriasl, R. Formability of aluminium alloy sheet at elevated temperature. *Thesis for DPhil degree in University of Waterloo*. 2012.
39. Ali, W.J., Jumah, O.T. Warm forming of aluminium alloy 2024 at different temperatures. *Al-Rafidain Engineering*. 2012, 20(2): 78-85.
40. Gao, H., Politis, D.J., Luan, X., Ji, K., Zhang, Q., Zheng, Y., Gharbi, M., Wang, L. Forming limit prediction for AA7075 alloys under hot stamping conditions. *J. Phys.: Conf. Ser*. 2017, 896 012089.
41. Li, F.F., Fu, M.W., Lin, J.P., Wang, X.N. Experimental and theoretical study on the hot forming limit of 22MnB5 steel. *Int. J. Adv. Manuf. Technol*. 2014, 71: 297-306.
42. Hussaini, S.M., Krishna, G., Gupta, A.K., Singh, S.K. Development of experimental and theoretical forming limit diagrams for warm forming of austenitic stainless steel 316. *J Manuf Process*. 2015, 18: 151-158.
43. Kathiravan, S., Sait, A.N., Ravichandran, M. Experimental investigation on stretchability of an austenitic stainless steel 316L. *Iranian J. Mater. Form*. 2016, 3(1), 55-64.
44. Gerdooei, M., Dariani, B.M., Liaghat, G.H. Effect of material models on formability of sheet metals in explosive forming. *Proceedings of the World Congress on Engineering*, WCE 2009, UK.
45. Palumbo, G., Tricarico, L. Numerical and experimental investigations on the warm deep drawing process of circular aluminium alloy specimens. *J. Mater. Process. Tech*. 2007, 184: 115-123.
46. Chu, X., Leotoing, L., Guines, D., Ragneau, E. Temperature and strain rate influence on AA5086 forming limit curves: experimental results and discussion on the validity of the M-K model. *Int. J. Mech. Sciences*. 2014, 78: 27-34.
47. Khan, A.S., Baig, M. Anisotropic responses, constitutive modeling and the effects of strain-rate and temperature on the formability of an aluminium alloy. *Int J. Plast*. 2011, 27: 522-538.
48. Abedrabbo, N., Pourboghrat, F., Carsley, J. Forming of AA5182-O and AA5754-O at elevated temperatures using coupled thermo-mechanical finite element models. *Int J. Plast*. 2007, 23: 841-875.
49. Chen, Z., Fang, G., Zhao, J. Formability evaluation of aluminum alloy 6061-T6 sheet at room and elevated temperatures. *J. Mater. Eng. Perform*. 2017, 26(9): 4626-4637.
50. Dicecco, S., Butcher, C., Worswick, M., Boettcher, E., Chu, E., Shi, C. Determination of forming limit diagrams of AA6013-T6 aluminum alloy sheet using a time and position dependent localized necking criterion. *IOP Conf. Ser. : Mater. Sci. Eng*. 2016: 159.
51. Shi, D.Y., Ying, L., Hu, P., Lu, J.D., Zhao, X., Liu, W.Q. Experimental and numerical determination of thermal forming limit diagrams (TFLD) of high strength steel 22MnB5. *AIP Conf. Proc*. 2013, 1532: 406-413.
52. Kolasangiani, K., Shariati, M., Farhangdoost, K. Prediction of forming limit curves (FLD, MSFLD and FLSD) and necking time for SS304L sheet using finite element method and ductile fracture criteria. *J. Comput. Appl. Res. Mech. Eng*. 2015, 4(2), 121-132.